

Digital Discovery

Accepted Manuscript

This article can be cited before page numbers have been issued, to do this please use: Y. Tang, B. Xiao, S. Chen, Q. Qian and Y. Liu, *Digital Discovery*, 2025, DOI: 10.1039/D5DD00079C.



This is an Accepted Manuscript, which has been through the Royal Society of Chemistry peer review process and has been accepted for publication.

Accepted Manuscripts are published online shortly after acceptance, before technical editing, formatting and proof reading. Using this free service, authors can make their results available to the community, in citable form, before we publish the edited article. We will replace this Accepted Manuscript with the edited and formatted Advance Article as soon as it is available.

You can find more information about Accepted Manuscripts in the [Information for Authors](#).

Please note that technical editing may introduce minor changes to the text and/or graphics, which may alter content. The journal's standard [Terms & Conditions](#) and the [Ethical guidelines](#) still apply. In no event shall the Royal Society of Chemistry be held responsible for any errors or omissions in this Accepted Manuscript or any consequences arising from the use of any information it contains.

Predefined attention-focused mechanism using center-environment features:

A machine learning study of alloying effects on stability of Nb₅Si₃ alloys

Yuchao Tang^{1, 2}, Bin Xiao¹, Shuizhou Chen³, Quan Qian³, and Yi Liu^{*1}

¹Materials Genome Institute, Shanghai Engineering Research Center for Integrated Circuits and Advanced Display Materials, Shanghai University, Shanghai 200444, China

²State Key Laboratory of Functional Materials for Informatics, Shanghai Institute of Micro-system and Information Technology, Chinese Academy of Sciences, Shanghai 200050, China

³School of Computer Engineering & Science, Shanghai University, Shanghai, 200444, China

*Corresponding author: yiliu@shu.edu.cn (Yi Liu)

Abstract:

Digital encoding of material structures using graph-based features combined with deep neural networks often lacks local specificity. Additionally, incorporating a self-attention mechanism increases architectural complexity and demands extensive data. To overcome these challenges, we developed a Center-Environment (CE) feature representation—a less data-intensive, physics-informed predefined attention mechanism. The pre-attention mechanism underlying the CE model shifts attention from complex black-box machine learning (ML) algorithms to explicit feature models with physical meaning, reducing data requirements while enhancing the transparency and interpretability of ML models. This CE-based ML approach was employed to investigate the alloying effects on the structural stability of Nb₅Si₃, with the objective of guiding data-driven compositional design for ultra-high-temperature NbSi superalloys. The CE features leveraged the Atomic Environment Type (AET) method to characterize the local low-symmetry physical environments of atoms. The optimized CE_{AET} models reasonably predicted double-site substitution energies in α-Nb₅Si₃, achieving a mean absolute error (MAE) of 329.43 meV/cell. The robust transferability of the CE_{AET} models was demonstrated by their successful prediction of untrained β-Nb₅Si₃ structures. Site occupancy preferences were identified for B, Si, and Al at Si sites, and for Ti, Hf, and Zr at Nb sites within β-Nb₅Si₃. This CE-based ML approach represents a broadly applicable and intelligent computational design method, capable of handling complex crystal structures with strong transferability, even when working with small datasets.

Keywords: Machine learning, Center-Environment feature engineering, Atomic Environment Type, NbSi-based superalloys, Structural Stability.



1. Introduction

Nb-Si based superalloys with high melting point and low density are expected to overcome the working temperature barrier of Ni-based superalloys, and have been extensively studied as a new generation of high-temperature structural materials¹. It contains a large number of high temperature intermetallic compounds Nb₅Si₃, which have high melting point (2520 °C), moderate density (7.16 g/cm³), high temperature strength and good creep resistance^{2,3}. However, single Nb₅Si₃ is brittle at room temperature, which seriously hinders its practical application^{3,4}. Nb₅Si₃ has both metal and ceramic properties, and its intrinsic brittleness at room temperature can be improved by alloying elements. Numerous experimental works have shown that adding alloying elements is an effective way to improve the comprehensive performance of Nb-Si alloys^{5–10}. The alloying elements that have been reported to be incorporated in NbSi-based alloys encompass a range of metals such as Ti¹¹, Cr¹², Al¹³, Hf¹⁴, Sn, Mo, W¹⁵, V, Ta, Fe, Zr, Ho¹⁶, Sr¹⁷, B¹⁸. It is time-consuming and labor-intensive only by trial-and-error experiments, while the calculation method based on first-principles can effectively predict the types of alloying elements and provide guidance for alloy composition design.

Chen *et al.*¹⁹ studied the atomic occupation positions of transition group metals in different sublattices of Nb₅Si₃. Their findings indicate that atoms with larger radii than Nb tend to occupy Nb_{II} sites, whereas atoms with smaller radii than Nb tend to occupy Nb_I sites in α -Nb₅Si₃. Xu *et al.*²⁰ studied the effects of vacancy concentration and Al substitution on the structural, electronic and elastic properties of Nb₅Si₃ by first-principles calculation. Guo *et al.*²¹ systematically studied the effect of Ag addition on the structure, mechanical and thermodynamic properties of α -Nb₅Si₃. Tsakiroopoulos *et al.*²² investigated the stability and physical properties of Ti doped α -Nb₅Si₃, β -Nb₅Si₃ and γ -Nb₅Si₃ alloys at different temperatures and concentrations. Xu *et al.*²³ determined the temperature-dependent structural properties and anisotropic thermal expansion coefficients of α -/ β -Nb₅Si₃ phases by minimizing the nonequilibrium Gibbs free energy as a function of crystal deformation. Shi *et al.*²⁴ focused on the effect of alloying elements on the mechanical properties and electronic structure of α -Nb₅Si₃. Kang *et al.*²⁵ investigated the energy, lattice parameters, electronic structure and elastic constants of Ti, Cr, Al and Hf doping in β -Nb₅Si₃. So far, the first-principles calculations focus on only a few elements and single-site substitution of NbSi-alloys



1 limited by cost. It is still far from adequate for screening alloying elements considering
2 the complex phase structure and wide range of alloying elements in multi-component
3 NbSi-based superalloys.

4 Machine learning as an emerging data-driven research paradigm in materials
5 science has proven to be effective and efficient in characterizing the complex structure-
6 property relationships of materials^{26–30}. It is well known that the properties of a material
7 were determined by both its chemical composition and structure, and thus ML features
8 should comprehensively characterize both, rather than focusing only on the
9 composition itself. To this end, Liu's group^{31–36} develops a Center-Environment (CE)
10 feature model that integrates both compositional and structural information into ML
11 features by mapping basic physicochemical properties onto a “core-shell” structural
12 framework. The CE feature model takes into account the properties of the ambient
13 atoms surrounding the central atom and quantifies the effect of the environment on the
14 central atom. The CE feature models have been successfully applied to predict a variety
15 of physicochemical properties of spinel oxide^{31,36}, perovskite oxide^{32,35}, metals³³ and
16 surface structures³⁴, including formation energies, lattice parameters, band gaps,
17 surface adsorption energies, and overpotentials for surface oxygen reactions.

18 In this study, the Nb₅Si₃ crystal structure exhibits low symmetry, possessing four
19 non-equivalent sites and a slightly distorted local environment. The traditional method
20 of defining nearest neighbor (NN) environment atoms encounters difficulties for local
21 low-symmetry distorted configuration, as these environment atoms were not easily
22 predetermined under different truncation conditions. Simply increasing the number of
23 NN environment atoms does not necessarily improve the accuracy of the prediction,
24 but may instead introduce redundant information with redundant negative effects. This
25 is because CE is essentially a localized feature representation, and too large a truncation
26 range may interfere with the accuracy of other localized CE atom sets. Therefore, a
27 proper general definition of the environment atoms becomes particularly important
28 when constructing CE features, especially for complex crystal structures. This is the
29 main driver of the methodological development in this work. The broader impact of
30 this work is that it provides an alternative to current graph-based neural network
31 methods, which have been limited in their application in materials science due to their
32 complex architecture and the need for large amounts of training data^{37–40}.

33 The conventional attention mechanism refers to the different weight parameters in
34 the deep neural networks of large language models. The optimization of weights



requires a large amount of data during the pre-trained stage that is normally not feasibly available in materials science. The CE feature model adopts a novel pre-attention mechanism that defines attention via the explicit feature models with physical meaning rather than the optimization of weights in complex black-box machine learning algorithms. This strategy can decrease data requirements and increase the transparent interpretability of ML models.

Aiming to accelerate the extended studies of new alloying elements and structures, the ML methods were developed in this work based on the previous first-principles computational data⁴¹ to investigate the structural stability properties of the alloyed α -Nb₅Si₃ phases. First, we developed the improved CE feature model, specifically adapted for low-symmetry crystals, by examining the different definitions of environment atoms and weights in the compound feature construction. Then, different ML algorithms were examined to obtain the optimal models of α -Nb₅Si₃ phases. The optimized ML models of α -Nb₅Si₃ were then used without modification to predict the substitution energies in new structures of high-temperature phase β -Nb₅Si₃ that were not included in the original training dataset, partially confirmed further by the first-principles calculations.

2. Models and Methods

2.1 Training dataset

The training dataset are built based on the first-principles calculations on the alloyed α -Nb₅Si₃⁴¹. Fig. 1 depicts the experimental structures of α -Nb₅Si₃ (body-centered tetragonal, BCT) crystals with the lattice parameters taken from the Materials Platform for Data Science (MPDS)⁴². The conventional cell of α -Nb₅Si₃ has two inequivalent Nb sites (dubbed Nb_I and Nb_{II}) and two inequivalent Si sites (dubbed Si_I and Si_{II}) for substitutions with alloying elements. In total, the 32-atom conventional cell consists of 20 Nb atoms and 12 Si atoms with four Nb_I, 16 Nb_{II}, 4 Si_I, and 8 Si_{II} atoms, respectively.



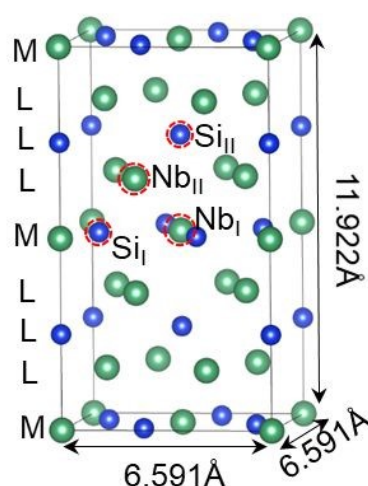


Fig. 1 Conventional cells of α -Nb₅Si₃ (BCT) crystal structures. The lattice parameters and inequivalent atom types are labeled. The stacking order of the atomic layers of α -Nb₅Si₃ is MLLL-MLLL along the longest axis where M and L indicate more closely packed and less closely packed layers, respectively.

Considering the double-site substitutions at the non-equivalent site pairs with 14 alloying elements, we collected 3528 double-site substitution energies (E_{DS}) data in α -Nb₅Si₃ phase from the literature⁴¹. We also calculated the incremental single-site substitution energy (E_{SS}) in the cases of double-site substitution and the local bond length change $\langle \Delta d \rangle$ as defined in Text S1 of Supplementary Materials (SM). The term "substitution energy" denotes the energy change associated with the replacement of alloying constituents. It is characterized as an incremental formation energy, measuring the stabilities of the site and phase occupancy of alloying elements. The configurations of the studied substitution pair sites were depicted in Fig. S1 for α -Nb₅Si₃. The statistics of the numbers of corresponding substitution systems were listed in Table S1. Fig. S2 (a-c) shows the statistical distributions of the target property data in α -Nb₅Si₃ that all satisfy the gaussian distributions. Fig. S3 indicates the 14 substitution alloying elements in the periodic table.

2.2 Center-Environment feature model

The CE features, which encode local structural and compositional information, have been proven effective in the study of alloys, oxides, and surface catalysis reactions^{31–34}. Considering the complex substitutional structure and lower symmetry of Nb₅Si₃ alloys, this study employs a CE feature model based on composition-structure characteristics. The CE feature model can be described as an (n+1)-dimensional



1 composite feature vector, as follows:

View Article Online
DOI: 10.1039/D5DD00079C

$$2 \quad D = [D_1, \dots, D_i, \dots, D_n, f], \text{ (e.g., } n = 20 \text{ in this work)} \quad (1)$$

3 D consists of a set of n elementary features of element (D_i) and the target property
4 f . D_i is a two-dimensional vector of the i th elementary property including the center
5 and environment components defined as follows:

$$6 \quad D_i = [d_{C,i}, d_{E,i}], i = 1, 2, \dots, n \quad (2)$$

$$7 \quad d_{C,i} = p_{C,i} \quad (3)$$

$$8 \quad d_{E,i} = \sum_{j=1}^N \omega_{E,j} p_{E,j,i} \quad (4)$$

$$9 \quad \omega_{E,j} = \frac{r_j^m}{\sum_{j=1}^N r_j^m} (m = -1, -\frac{1}{2}) \quad (5)$$

10 where C and E represent the center atoms and environment atoms, respectively; i is the
11 elementary property index and j is the index of environment atoms. $p_{C,i}$ is the i -th
12 elementary property of the center atom; $p_{E,j,i}$ is the i -th property of the j -th
13 environment atom around the center atom; $\omega_{E,j}$ denotes the normalized weight of
14 elementary properties as functions of distance r_j between the center atom and the j -th
15 environment atom. The weight is inversely proportional to the distance as r_j^m (m
16 $= -1, -1/2$) where different powers m was studied and compared in this work.

17 It is well known that feature engineering determines the accuracy of ML modeling
18 ^{31,43–46}. The CE features were compound features consisting of an assembly of
19 elementary property features encoded with local structural information specified by the
20 center and environment atoms: (1) Elementary property features are various elementary
21 physicochemical properties readily available from the fundamental database⁴⁷, e.g.,
22 atomic mass, radius, electronegativity, and the number of valence electrons of elements
23 as well as density, melting temperature, and bulk modulus of pure substance among
24 others. In total 40 elementary properties were adopted in the feature construction as
25 listed in Table S2. (2) Compound property features are constructed by a linear
26 combination of the elementary properties of the center atom or the environment atoms
27 with weights inversely proportional to the distance between the center atom and the
28 environment atom (r_j^m , $m = -1, -1/2$). The exponent m in the decay function measures
29 how quickly environmental effects diminish with distance. By this way, CE features
30 can encode the elementary properties with the local composition and structure
31 information, providing a general digital representation of materials structure.

32 The design concepts of CE model include:



(1) Localized focus: CE features explicitly define the interaction weights between the central atom and its neighboring environment through the Atomic Environment Type (AET) method. The pre-defined attention via “core-shell” configuration allows the accurate local representation without the needs of a large amount of data for global representation.

(2) Distance-weighted interactions: By employing decay functions based on interatomic distances, the CE method pre-define the weight allocation process reflecting center-environment interactions. The reciprocal distance dependent decay function can be attributed to the electrostatic interaction of Coulomb’s law.

In contrast to the CE feature models, the Chemical Composition (CC) feature models focus solely on chemical composition without considering structural information. The construction of CC feature is similar to that of CE except that the weight r_j^m ($m = 0$) is independent of distance (see more details in Text S2).

2.3 Machine learning algorithms and evaluation

For this study, machine learning uses the Support Vector Regression (SVR) algorithm with an isotropic radial basis function (RBF)⁴⁸ kernel, and the Random Forest algorithm (RF)⁴⁹, both efficiently implemented via Python’s Scikit-learn library. To enhance model performance, we meticulously fine-tuned the hyperparameters of both SVR and RF using a grid search approach. The optimized hyperparameters are listed in Table S3, with corresponding discussions and analyses elaborated in Text S3.

First, we executed a randomized split of the entire original dataset into a training set and a test set with an 8:2 ratio. The training set then underwent 20 iterations of 5-fold cross-validation, with each fold adhering to the 8:2 partition ratio. The test set, comprising 20% of the original data, was independently retained to evaluate the performance of the trained ML models, ensuring it was not utilized during the training stage. To evaluate the performance of the regression models, the statistical metrics used were correlation coefficient (R^2), mean absolute error (MAE) and root mean square error (RMSE). These evaluation metrics were defined below:

$$R^2 = 1 - \frac{\sum_{j=0}^{n-1} (\hat{y}_j - y_j)^2}{\sum_{j=0}^{n-1} (\bar{y} - y_j)^2} \quad (6)$$

$$E_{MAE} = \frac{1}{n} \sum_{j=1}^n |y_j - \hat{y}_j| \quad (7)$$

$$E_{RMSE} = \sqrt{\frac{1}{n} \sum_{j=1}^n (y_j - \hat{y}_j)^2} \quad (8)$$

where n is the number of samples; y_j is the true value; \hat{y}_j is the predicted value; \bar{y}



is the mean of predicted values.

View Article Online
DOI: 10.1039/D5DD00079C

3. Results and discussion

3.1 Machine learning models

3.1.1 CE_{NN} and CE_{AET} feature models

The CE feature model essentially provides a center and environment framework of encoding local composition and structure information of materials. The center atoms are normally the focused atoms, e.g., the substitution alloying elements at the non-equivalent sites Nb_I , Nb_{II} , Si_I , and Si_{II} of α - Nb_5Si_3 in this work. It is physically necessary to consider the effects of environment atoms on the center atoms. The definition of environment atoms is critical to the appropriate representation of local chemical and structural information. To explore the impact of the environment atoms on the performance of ML-CE models, we developed two construction methods of environment atoms described as follows.

(I) Nearest neighbor (dubbed CE_{NN}) feature model. For crystalline materials with high symmetry, such as FCC or BCC structures, the selection of environment atoms based on the distances from the center atom to its surroundings is inherently straight forward. In this model, environmental atoms are defined as the n th-nearest neighbors to the central atom. The environmental atoms in the alloyed α - Nb_5Si_3 systems were identified up to the fifth nearest neighbors, with a distinction at the Nb_{II} center atom of α - Nb_5Si_3 , where the inclusion extended to the 10th nearest neighbors.

(II) Atomic Environment Type (dubbed CE_{AET}) feature model. For crystal structures with low symmetry, e.g., α - Nb_5Si_3 , the distance based cutoff definition is no longer appropriate to describe the environment. Therefore, this work employs a physics-based definition of the atomic environment to construct the CE features, utilizing the concept of AET proposed by Villars⁵⁰ for classification of inorganic compounds. The AET represents a complete enclosed physical shell surrounding the central atom based on the geometric topology rather than just distance cutoffs. To qualify as AET environmental atoms, two rules must be satisfied: the maximum distance gap (MDG) and the convex volume (CV). The MDG rule requires that AET atoms have the maximum gap in the nearest-neighbor histogram (NNH), which is a plot of the number (n) of certain interatomic distances (d) as a function of the normalized distances (d/d_{min}) between the central atom and surrounding atoms. The second CV rule



mandates that AET atoms must enclose a convex polyhedral shape. Fig. 2 depicts the AET cluster models and their NNHs with the centers of non-equivalent sites in α -Nb₅Si₃. Fig. 2 shows the AET cluster models around the four non-equivalent sites of α -Nb₅Si₃: Nb_I (CN= 14, code: 8^{0.3}6^{0.4}), Nb_{II} (CN= 16, code: 12^{5.0}4^{6.0}), Si_I (CN= 9, code: 3^{4.0}6^{5.0}), and Si_{II} (CN= 10, code: 8^{5.0}2^{4.0}) where CN represents coordination number. The AET code encodes the structure's topology by listing the counts of polygons (triangles, squares, pentagons, hexagons) at each vertex. For example, in Fig. 2(a), a CN of 14 is the sum of 8 and 6, indicating 8 vertices connected to 3 squares and 6 to 4 squares, with no triangles. This scheme effectively quantifies local polygonal arrangements and coordination environments, offering a detailed topological characterization. The local atomic structures of α -Nb₅Si₃ exhibit low symmetry as indicated by the distorted polyhedron. For example, the AET cluster around Nb_{II} site has up to the 9th nearest neighbor atoms with a maximum distance gap from the 10th nearest neighbor atoms by counting the distributions in nearest-neighbor histogram (NNH) in Fig. 2(b). The numbers of AET atoms vary depending on the local symmetry so it is hard to predefine the *n*th nearest neighbors without careful check in advance. The inappropriate choice

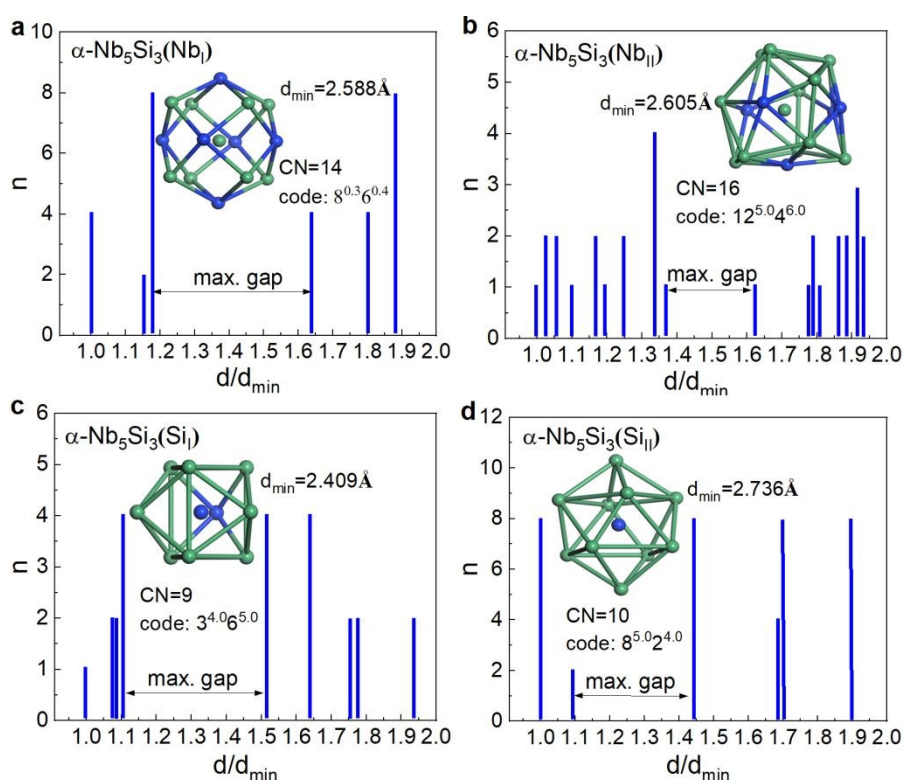


Fig. 2 Nearest-neighbor histogram (NNH) of α -Nb₅Si₃ around the four non-equivalent sites: **a** Nb_I (CN= 14, code: 8^{0.3}6^{0.4}), **b** Nb_{II} (CN= 16, code: 12^{5.0}4^{6.0}), **c** Si_I (CN= 9, code: 3^{4.0}6^{5.0}), **d** Si_{II} (CN= 10, code: 8^{5.0}2^{4.0}). The insets are the Atomic Environment Type (AET) cluster models (Nb atoms in green and Si atoms in blue).



of the n th nearest neighbors as the environment atoms will lead to an incomplete or redundant shell atoms and physically less meaningful features in the CE feature construction. The performance of ML models using CE_{NN} and CE_{AET} features will be evaluated and compared later.

3.1.2 Performance evaluation of various ML models

To compare the prediction accuracy of different ML models, we show the performance metrics of the CE_{NN} , CE_{AET} , and CC feature models with different weights and parameter settings of various algorithms for $\alpha\text{-Nb}_5\text{Si}_3$ in Table S4-S10 and Fig. S4-S7.

The SVR algorithm (Fig. 3) exhibited generally more accurate prediction by ~ 100 – 200 meV/cell than the RF algorithm with all studied features so that the SVR results were mainly used for discussion. The CE feature models (Table S4, S5) performed much better than the composition CC models (Table S6), indicating that the inclusion of structural information into the feature construction via CE framework is critical to describing the complex crystal structures by ML methods. Furthermore, the CE_{AET} models using the AET environment atoms had better prediction accuracy than the CE_{NN} models using the nearest-neighbor atoms even though more atoms may be included in the latter cases (Fig. 3). This suggests that the physically closed shell is more appropriate to define ML features than the distance-based cutoff selection possibly with either insufficient or redundant environment atoms. Comparison among the CE_{AET} feature models, the weight r_j^{-1} performs mostly better than $r_j^{-1/2}$ (Fig. 3), indicating that the linear combination of elementary property features with the weight of reciprocal distance is a reasonable choice probably due to the scaling law of long-range electrostatic interactions in Coulomb's law. Based on the comparisons above, the

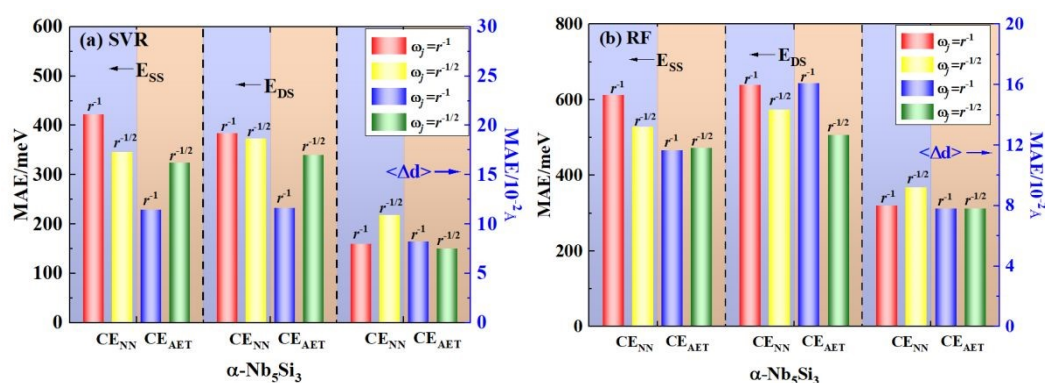


Fig. 3 MAE of prediction of $\alpha\text{-Nb}_5\text{Si}_3$ by the SVR and RF methods using CE_{NN} and CE_{AET} feature models with different weights r_j^m ($m = -1, -1/2$).





1 CE_{AET}-SVR models with weight $w_j = 1/r$ were mainly used to predict the target
2 properties (E_{SS} , E_{DS} , and $\langle \Delta d \rangle$) of new datasets in α -Nb₅Si₃ hereafter. Although the
3 other algorithms like GBR, LGBM, and XGB achieve high accuracy with limited
4 samples (Table S11), their predictions are still less precise than SVR. In cross-
5 validation, SVR shows better generalization, likely due to its kernel function's
6 suitability for high-dimensional small data.

7 Table 1 shows the prediction results of different ML models for the substitution
8 energies at the four nonequivalent sites (Nb_I, Nb_{II}, Si_I, and Si_{II}) of α -Nb₅Si₃ in the
9 independent test datasets. Comparing the ML results of four non-equivalent sites
10 substitutions, it is found that the graph-based deep learning model 3D-ELAN and the
11 non-deep learning model CE_{AET}-SVR achieved $\langle R^2 \rangle$ values both higher than 0.9.
12 Specifically, the $\langle MAE \rangle$ values predicted by the 3D-ELAN model for the substitution
13 energies of the four non-equivalent sites of α -Nb₅Si₃ are 248.80 meV, 307.60 meV,
14 419.20 meV, and 301.20 meV per supercell, respectively. The prediction had very large
15 errors using the other popular graph-based feature models including GCN, GAT, and
16 ALIGNN. In contrast, the optimal non-deep machine learning model, CE_{AET}-SVR, have

Table 1 Prediction performances of substitution energies of α -Nb₅Si₃ alloys using CE features model and other deep machine learning models in the literatures.

Models	Performance	Non-equivalent sites				All sites
	metric	Nb _I	Nb _{II}	Si _I	Si _{II}	
GCN ³²	$\langle R^2 \rangle$	0.64	0.49	0.67	0.52	—
	$\langle RMSE \rangle$ (meV)	943.60	999.01	956.80	973.30	—
	$\langle MAE \rangle$ (meV)	644.80	513.00	625.10	681.00	—
GAT ³³	$\langle R^2 \rangle$	0.27	0.45	0.04	0.04	—
	$\langle RMSE \rangle$ (meV)	1321.40	1031.70	1620.20	1377.20	—
	$\langle MAE \rangle$ (meV)	1059.70	727.01	1330.31	1108.82	—
ALIGNN ³⁴	$\langle R^2 \rangle$	-0.03	0.10	0.12	0.11	—
	$\langle RMSE \rangle$ (meV)	1573.30	1317.90	1553.01	1334.10	—
	$\langle MAE \rangle$ (meV)	1275.50	1075.60	1264.32	1040.50	—
3D-ELAN	$\langle R^2 \rangle$	0.96	0.93	0.94	0.90	—
	$\langle RMSE \rangle$ (meV)	336.50	394.70	584.10	428.30	—
	$\langle MAE \rangle$ (meV)	248.80	307.60	419.20	301.20	—
CE _{AET} -RF	$\langle R^2 \rangle$	0.85	0.82	0.95	0.92	0.81
	$\langle RMSE \rangle$ (meV)	591.56	574.10	449.18	459.25	780.35
	$\langle MAE \rangle$ (meV)	391.11	454.11	347.70	359.95	578.16
CE _{AET} -SVR	$\langle R^2 \rangle$	0.96	0.97	0.98	0.99	0.93
	$\langle RMSE \rangle$ (meV)	263.89	271.01	268.80	115.34	465.83
	$\langle MAE \rangle$ (meV)	137.95	177.35	174.86	71.39	329.43

the best performance with $\langle \text{MAE} \rangle$ values of 137.95, 177.35, 174.86, and 71.39 meV/cell for the same substitution energies.

Based on the prediction of the four non-equivalent sites, we further modeled and predicted the substitution energies for all sites in $\alpha\text{-Nb}_5\text{Si}_3$. The results indicated that the non-deep machine learning model $\text{CE}_{\text{AET-SVR}}$ outperformed $\text{CE}_{\text{AET-RF}}$, with predicted $\langle \text{MAE} \rangle$ values of 329.43 and 578.16 meV/cell, respectively. Notably, the errors for the four inequivalent sites are larger than any single substitution site because of the different center-environment configurations. The hundreds of meV of MAE is larger than conventional formation energies of bulk crystal because the prediction of diverse local substitutions in this work is much more challenging than traditional studies of global substitution in bulk crystals.

3.2 Construction of machine learning models in $\alpha\text{-Nb}_5\text{Si}_3$

In the crystal structure of $\alpha\text{-Nb}_5\text{Si}_3$, the four non-equivalent sites, Nb_{I} , Nb_{II} , Si_{I} , and Si_{II} , have different AET environment atoms, so we constructed the machine learning models for the substitution systems at the four non-equivalent sites, respectively.

Fig. 4 shows the E_{SS} , E_{DS} , and $\langle \Delta d \rangle$ of the $\alpha\text{-Nb}_5\text{Si}_3$ substitution systems at the four non-equivalent sites Nb_{I} , Nb_{II} , Si_{I} , Si_{II} , and all sites predicted by the optimal $\text{CE}_{\text{AET-SVR}}$ models compared with the DFT results.

The predictive performance across different sites in $\alpha\text{-Nb}_5\text{Si}_3$ shows high accuracy, with R^2 values generally above 0.9 and low $\langle \text{MAE} \rangle$ and $\langle \text{RMSE} \rangle$, indicating reliable energy predictions (Fig. 5). The models trained on a common feature set, incorporating different AET environments, demonstrate the broad applicability of the CE approach, though accuracy diminishes with increased system complexity. Overall, the substitution elements have minimal impact on local bond distances, with $\langle \Delta d \rangle$ remaining below 10^{-2} Å, suggesting that local structural variations are subtle across different substitution scenarios.



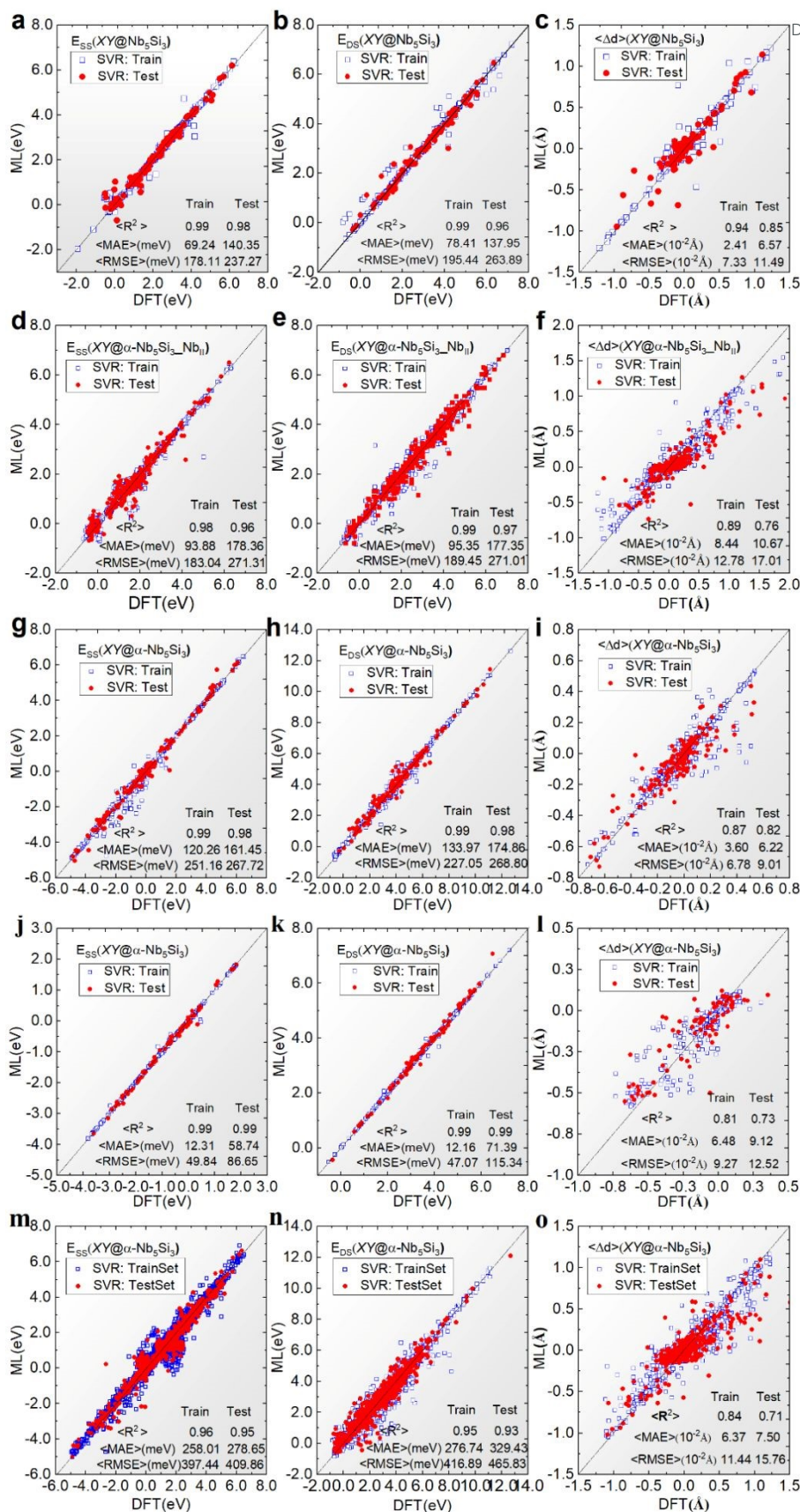


Fig. 4 E_{SS}, E_{DS}, and <Δd> of the α -Nb₅Si₃ substitution systems at the four non-equivalent sites (a-c) Nb_I, (d-f) Nb_{II}, (g-i) Si_I, (j-l) Si_{II}, and (m-o) all sites predicted by the CE_{AET}-SVR models compared with the DFT results.



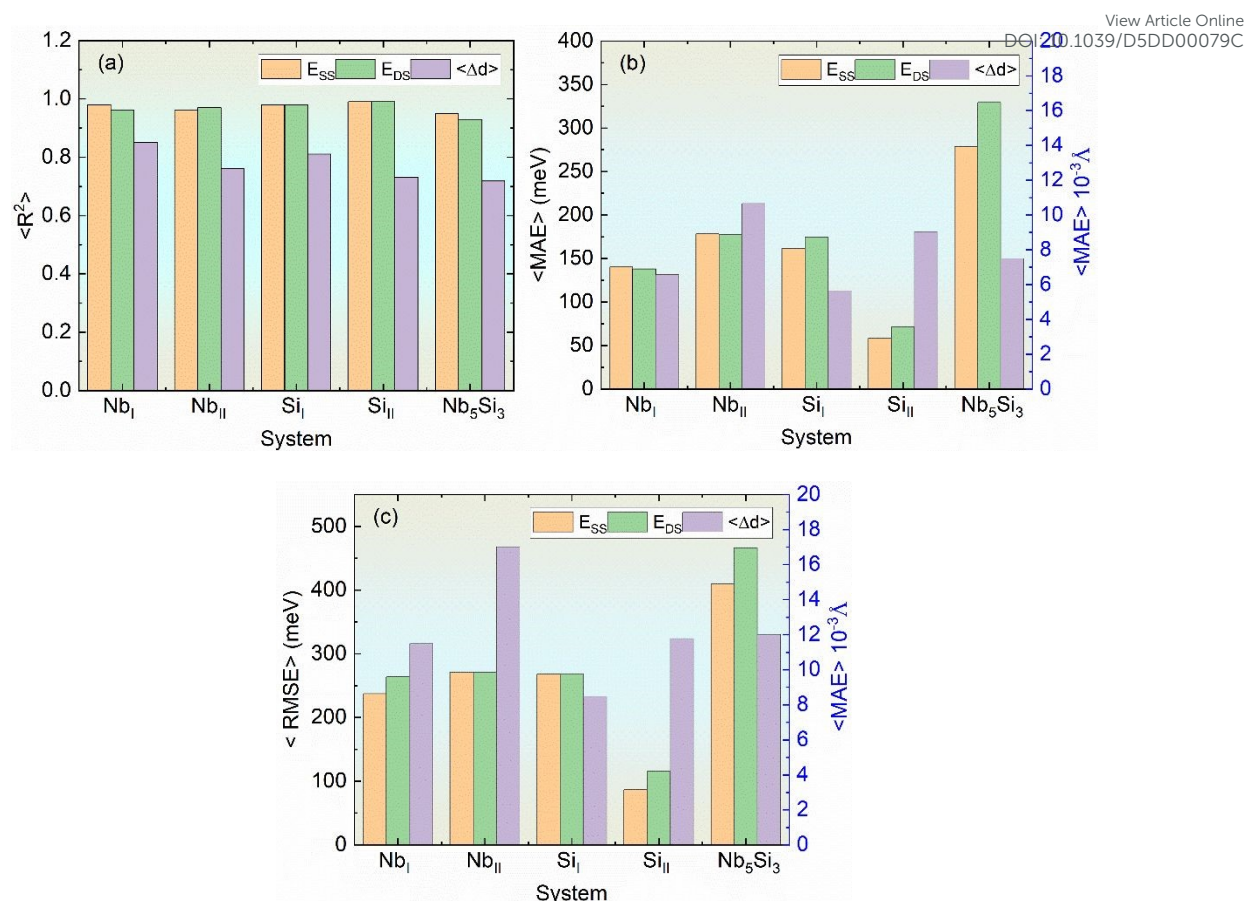


Fig. 5 Comparison of ML errors at different sites in $\alpha\text{-Nb}_5\text{Si}_3$: (a) $\langle R^2 \rangle$, (b) $\langle \text{RMSE} \rangle$, and (c) $\langle \text{MAE} \rangle$.

To understand the site dependence of substitution energies, we plot the heat maps of the double-site substitution energy E_DS projection on the substitution pair sites. The distribution patterns of substitution energy predicted by the ML are very similar to those of DFT, confirming the reliability of the ML predictions. Such site-energy heat maps help to find the stabilized element pairs quickly. Figures S8-S11 show the heat maps of the E_DS projection on different site pairs containing the non-equivalent sites Nb_I , Nb_II , Si_I , and Si_II in $\alpha\text{-Nb}_5\text{Si}_3$, respectively. The ML predicted distribution patterns are consistent with DFT. The B, Al, and Si elements preferred to occupy the Si sites, while Ti, Nb, Hf, and Zr tend to occupy Nb sites in $\alpha\text{-Nb}_5\text{Si}_3$. In summary, the machine learning method was validated against DFT and can be used to find new favorable stabilized alloying elements in NbSi-based superalloys next.

To enhance the interpretability and physical significance of the machine learning (ML) model, we employed SHAP (SHapley Additive exPlanations) methodology to analyze the contribution levels and influence trends of critical features in the optimal



ML model predicting dual-site substitution energy (E_{DS}) for Nb_5Si_3 superalloys. Fig. S12 presents the SHAP analysis of E_{DS} in $\alpha-Nb_5Si_3$. The feature importance ranking by SHAP values [Fig. S12(a)] reveals the top five most influential features: PN_C, BM_C, TN_C, EC_E, and DV_E. As detailed in Table S2, these features correspond to cohesive energy (EC), bulk modulus (BM), period number (PN), distance-valence moment (DV), and thermal neutron capture cross-section (TN), demonstrating their critical roles in the $\alpha-Nb_5Si_3$ model. Notably, all significant features originate from contributions of both central and environmental atoms. For fundamental properties of the same type, environmental atomic features depend simultaneously on elemental identity and spatial distance, while central atomic features in the CE framework solely depend on element type. This highlights the necessity of differentiating central and environmental atomic characteristics in feature construction for complex crystal structures. Furthermore, the $\alpha-Nb_5Si_3$ system requires structure-dependent environmental atomic features beyond basic chemical composition.

The SHAP value distributions [Fig. S12(b)] qualitatively illustrate the qualitative trends of feature impacts on substitution energy. In the $\alpha-Nb_5Si_3$ model, PN_C, BM_C, and TN_C exhibit positive correlations with substitution energy, whereas EC_E and DV_E show negative correlations. The inverse relationship between cohesive energy (EC) and substitution energy implies that higher cohesive energies correspond to more negative substitution energies. This correlation aligns with fundamental thermodynamic principles, as both increased cohesive energy and negative substitution energy values indicate enhanced system stability. The SHAP analysis in Fig. S12, reveals that the primary features influencing the substitution energy of $\alpha-Nb_5Si_3$ with dual-site substitution (e.g., PN_C, BM_C) originate from the synergistic contributions of the central and surrounding atoms. Notably, environmental atom features depend on both element type and spatial distance, whereas central atom features are exclusively determined by element type. These findings underscore the critical importance of differentiating atomic roles when constructing features for complex crystal structures.

3.3 Applications of machine learning models

After the construction, comparison, and validation of the ML models discussed above, the optimal CE_{AET} -SVR models with weight $w_j = 1/r$ were selected to study the unknown systems including new alloying elements and matrix alloys that were not in the training datasets. The ML applicability would significantly extend the prediction



1 capability and efficiency beyond expensive first-principles computations.

2 3.3.1 Leave-p-out prediction of new alloying elements

3 To examine the capability of the ML models to predict the energy and structure of
4 the new alloying elements, we predicted the E_{SS} , E_{DS} , and $\langle\Delta d\rangle$ for each of the 14
5 substituted alloying elements in the $\alpha\text{-Nb}_5\text{Si}_3$ phases using the leave-p-out cross
6 validation method. The “leave-p-out” tests mean that the p configurations containing
7 the specified type of element are used for independent tests while the others are used
8 for training. The value of p is 486, corresponding to 18 sites with 27 configurations at
9 each site in this work. Specifically, the full datasets containing the 14 elements were
10 split into the test datasets of a target element and the training datasets of the remaining
11 13 elements. In other words, the ML model trained with the 13-element dataset was
12 used to predict the properties of the 14th element. Such leave-one-out validation
13 procedures were performed for each of the 14 substitution elements. The R^2 and MAE
14 metrics of the leave-one-out ML prediction for the 14 alloying elements in $\alpha\text{-Nb}_5\text{Si}_3$
15 phases are shown in Fig. S13 and Fig. 6.

16 Fig. S13 shows the performance metrics of E_{DS} in $\alpha\text{-Nb}_5\text{Si}_3$ phase predicted by the
17 $\text{CE}_{\text{AET}}\text{-SVR}$ models. The $\langle R^2 \rangle$ of Al, Co, Fe, Mo, Nb, Ti, V, and Y reached 0.86, 0.90,
18 0.92, 0.87, 0.91, 0.93, 0.86, and 0.86, respectively. The corresponding $\langle \text{MAE} \rangle$ were
19 555.94, 351.43, 301.23, 483.88, 460.88, 425.88, 518.86, and 648.72 meV/cell,
20 respectively. The other elements had larger $\langle \text{MAE} \rangle$ with $\langle R^2 \rangle$ less than 0.85.

21 Fig. 6 summarizes the $\langle \text{MAE} \rangle$ of the substitution energies of $\alpha\text{-Nb}_5\text{Si}_3$ in the
22 leave-p-out prediction of each of the 14 alloying elements using $\text{CE}_{\text{AET}}\text{-SVR}$ models.
23 In the case of $\alpha\text{-Nb}_5\text{Si}_3$ phase, the $\langle \text{MAE} \rangle$ of Fe elements were less than 300 meV/cell,
24 and the $\langle \text{MAE} \rangle$ most elements were in 300~600 meV/cell, e.g. Y, Ti, Zr, V, Nb, Mo,
25 Al, and Co. While the $\langle \text{MAE} \rangle$ of B, Si, Hf, Cr, and Ni elements were greater than 600
26 meV/cell. It is crucial to bear in mind the prediction errors associated with new elements
27 when applying ML models. Specifically, larger prediction errors primarily involve
28 main group non-metals (B, Si) and elements with larger metallic radii, such as Hf,
29 highlighting their distinct characteristics compared to transition metals. The magnitude
30 of the $\langle \text{MAE} \rangle$ inversely correlates with the compatibility between substitution



elements and host sites — smaller MAE values indicate reduced discrepancies in physicochemical properties between substituents and their host lattice positions. The divisions of three error bands are used to cover the whole error ranges, which can serve as the quantitative metric of similarities among the various alloying effects.

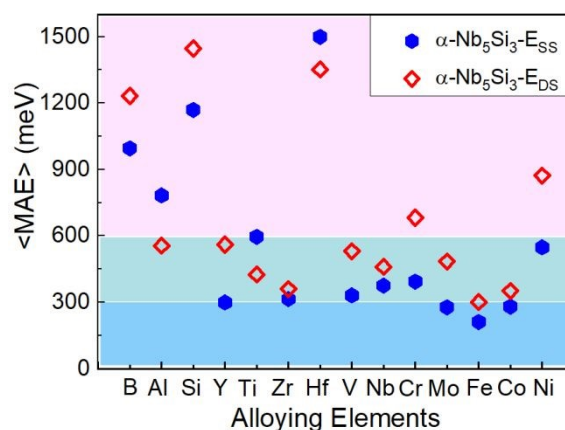


Fig. 6 $\langle \text{MAE} \rangle$ of the substitution energies in the leave-p-out prediction of each of the 14 alloying elements in $\alpha\text{-Nb}_5\text{Si}_3$ phase using $\text{CE}_{\text{AET}}\text{-SVR}$ models, respectively. The alloying elements are sorted by the number of valence electrons.

3.3.2 Prediction of new $\beta\text{-Nb}_5\text{Si}_3$ structure beyond training dataset

In the previous Section 3.3.1, we examined the ML predictions on the new substitution alloying elements of the same structures. Now we will examine the predictive capability of ML models on the new structures substituted with the same alloying elements without expensive DFT calculations.

The Nb-Si binary phase diagram shows that $\alpha\text{-Nb}_5\text{Si}_3$ is the stable phase at ambient conditions while $\beta\text{-Nb}_5\text{Si}_3$ is more stable at the high-temperature⁵¹. Prompting $\alpha\text{-}\beta$ phase transition at high-temperature operating conditions may improve the mechanical properties of Nb-Si alloys. Therefore, it is also interesting to find the alloying elements that can stabilize $\beta\text{-Nb}_5\text{Si}_3$ phase. The conventional cell of $\beta\text{-Nb}_5\text{Si}_3$ crystal structure has the lattice constants of $a = b = 10.06 \text{ \AA}$, $c = 5.07 \text{ \AA}$ (Fig. S14). The $\beta\text{-Nb}_5\text{Si}_3$ exhibits the body-centered tetragonal structure with four non-equivalent sites: Nb_{I} (CN= 14, code: $12^{5.0}2^{6.0}$), Nb_{II} (CN= 15, code: $12^{5.0}3^{6.0}$), Si_{I} (CN= 10, code: $2^{4.0}8^{5.0}$), and Si_{II} (CN= 10, code: $3^{4.0}6^{5.0}1^{6.0}$). Fig. 7 shows the NNH and AET cluster models of $\beta\text{-Nb}_5\text{Si}_3$ around the four non-equivalent sites. The local structures of $\beta\text{-Nb}_5\text{Si}_3$ are also complex, e.g., up to the 9th nearest-neighbor atoms are necessary to enclose the first physical shell around Nb_{II} site. The AET type definition of the environment atoms is generally



1 applicable to both α -Nb₅Si₃ and β -Nb₅Si₃ despite that their crystal structures are
 2 different.

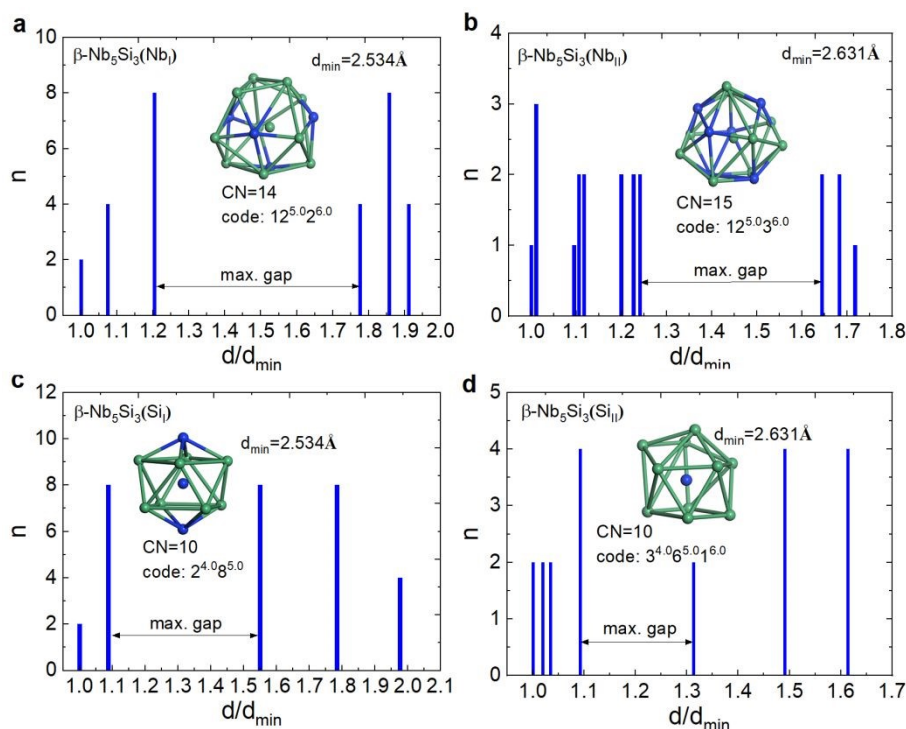


Fig. 7 Nearest-neighbor histogram (NNH) of β -Nb₅Si₃ around the four non-equivalent sites; (a) Nb_I (CN= 14, code: 12^{5.0}2^{6.0}), (b) Nb_{II} (CN= 15, code: 12^{5.0}3^{6.0}), (c) Si_I (CN= 10, code: 2^{4.0}8^{5.0}), and (d) Si_{II} (CN= 10, code: 3^{4.0}6^{5.0}1^{6.0}). The insets are the Atomic Environment Type (AET) cluster models (Nb atoms in green and Si atoms in blue).

The optimal CE_{AET}-SVR models were trained using all E_{DS} of α -Nb₅Si₃ substituted with the 14 alloying elements: B, Al, Si, Ti, V, Cr, Fe, Co, Ni, Y, Zr, Nb, Mo, and Hf. Then we applied these ML models directly to predict the E_{DS} of 784 double-site substitution systems of β -Nb₅Si₃ doped with the same set of alloying elements. Fig. 8 shows the heat map of E_{DS} projection on the four non-equivalent site pairs of β -Nb₅Si₃: $X_{NbI}Y_{NbII}$, $X_{NbI}Y_{SiI}$, $X_{NbII}Y_{SiI}$, and $X_{NbII}Y_{SiII}$ where $X, Y = B, Ni, Co, Fe, Si, V, Mo, Al, Ti, Nb, Hf, Zr$ and Y , sorted in the increasing order of metal radii.

The E_{DS} of the $X_{NbI}Y_{NbII}$ @ β -Nb₅Si₃ systems were all positive [Fig. 8 (a)], indicating that the substitutions at the Nb_INb_{II} site of β -Nb₅Si₃ were energetically not favorable. The relative preference of occupation in β -Nb₅Si₃ were similar to those of α -Nb₅Si₃: Ti, Hf, and Zr were more readily to occupy Nb_INb_{II} sites than B, Si, Al, and Y. The alloying elements exhibit similar occupancy tendencies at the other three substitution sites of β -Nb₅Si₃, including all Nb-Si pairs: $X_{NbI}Y_{SiII}$, $X_{NbII}Y_{SiI}$, and



1 $X_{\text{NbII}}Y_{\text{SiII}}$ [Fig. 8 (b)-(d)]. Specifically, B, Si, and Al prefer to occupy Si_I or Si_II sites, while Ti, Hf, and Zr tend to occupy Nb_I or Nb_II sites. The occupancy tendency at the NbSi sites of $\beta\text{-Nb}_5\text{Si}_3$ is consistent with that of $\alpha\text{-Nb}_5\text{Si}_3$. The substitution pairs that stabilized $\beta\text{-Nb}_5\text{Si}_3$ with negative substitution energies were $\text{Hf}_{\text{NbI}}\text{B}_{\text{SiII}}$ (-0.61 eV), $\text{Ti}_{\text{NbI}}\text{B}_{\text{SiII}}$ (-0.34 eV), and $\text{Zr}_{\text{NbI}}\text{B}_{\text{SiII}}$ (-1.09 eV) at $X_{\text{NbI}}Y_{\text{SiII}}$ sites; $\text{Zr}_{\text{NbII}}\text{B}_{\text{SiI}}$ (-0.05 eV) and $\text{Hf}_{\text{NbII}}\text{B}_{\text{SiI}}$ (-0.17 eV) at $X_{\text{NbII}}Y_{\text{SiI}}$ sites; $\text{Hf}_{\text{NbII}}\text{B}_{\text{SiII}}$ (-0.72 eV), $\text{Hf}_{\text{NbII}}\text{Si}_{\text{SiII}}$ (-0.67 eV), $\text{Ti}_{\text{NbII}}\text{B}_{\text{SiII}}$ (-0.95 eV), $\text{Ti}_{\text{NbII}}\text{Si}_{\text{SiII}}$ (-0.78 eV), and $\text{Zr}_{\text{NbII}}\text{B}_{\text{SiII}}$ (-0.28 eV) at $X_{\text{NbII}}Y_{\text{SiII}}$ sites. These results suggest that Ti, Zr, and Hf are stabilizing elements at the Nb sites of $\beta\text{-Nb}_5\text{Si}_3$ and may be better co-doped with B at the Si sites.

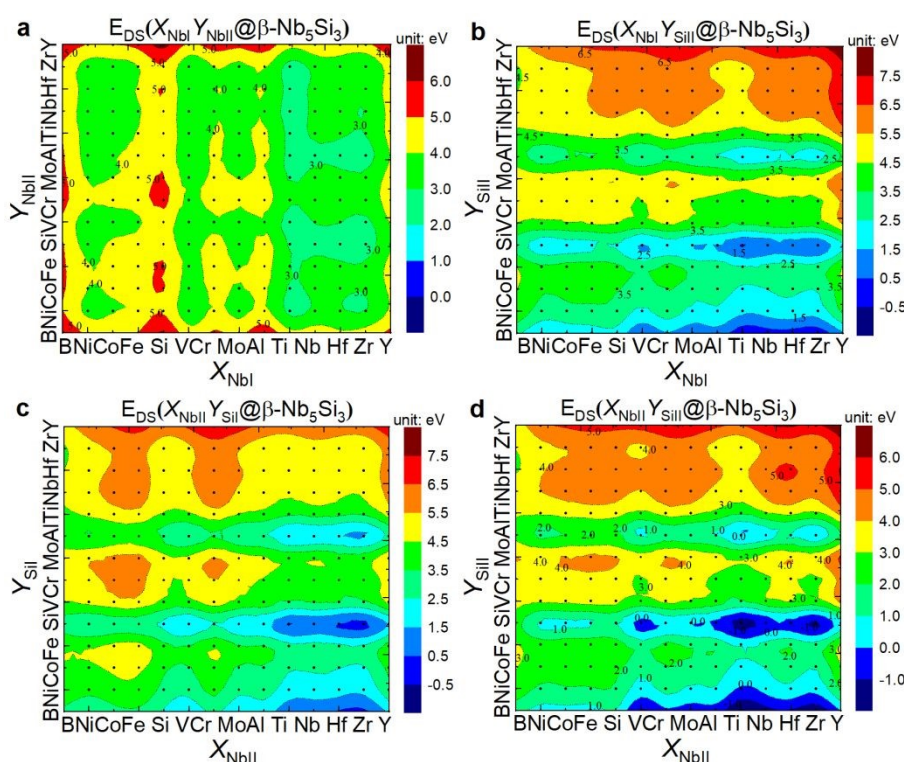


Fig. 8 Double-site substitution energies (E_{DS}) of $\beta\text{-Nb}_5\text{Si}_3$ predicted by the $\text{CE}_{\text{AET}}\text{-SVR}$ models that were originally trained for $\alpha\text{-Nb}_5\text{Si}_3$. The heat map of E_{DS} projection on the four non-equivalent site pairs of $\beta\text{-Nb}_5\text{Si}_3$: (a) $X_{\text{NbI}}Y_{\text{NbII}}$, (b) $X_{\text{NbI}}Y_{\text{SiII}}$, (c) $X_{\text{NbII}}Y_{\text{SiI}}$, and (d) $X_{\text{NbII}}Y_{\text{SiII}}$ where $X, Y = \text{B, Ni, Co, Fe, Si, V, Mo, Al, Ti, Nb, Hf, Zr}$ and Y , sorted in the increasing order of metal radii.

10 To validate the E_{DS} of $\beta\text{-Nb}_5\text{Si}_3$ predicted by the ML models that were originally
 11 trained for $\alpha\text{-Nb}_5\text{Si}_3$, we performed DFT calculations on the stabilized $\beta\text{-Nb}_5\text{Si}_3$
 12 systems suggested by the ML models. The E_{DS} of $\beta\text{-Nb}_5\text{Si}_3$ calculated by DFT were
 13 $\text{Hf}_{\text{NbI}}\text{B}_{\text{SiII}}$ (-0.19 eV), $\text{Ti}_{\text{NbI}}\text{B}_{\text{SiII}}$ (-0.49 eV), and $\text{Zr}_{\text{NbI}}\text{B}_{\text{SiII}}$ (-0.55 eV) at $X_{\text{NbI}}Y_{\text{SiII}}$ sites;
 14 $\text{Zr}_{\text{NbII}}\text{B}_{\text{SiI}}$ (-0.03 eV) and $\text{Hf}_{\text{NbII}}\text{B}_{\text{SiI}}$ (-0.09 eV) at $X_{\text{NbII}}Y_{\text{SiI}}$ sites; $\text{Ti}_{\text{NbII}}\text{B}_{\text{SiII}}$ (-0.44 eV),
 15 $\text{Ti}_{\text{NbII}}\text{Si}_{\text{SiII}}$ (-0.31 eV), $\text{Hf}_{\text{NbII}}\text{B}_{\text{SiII}}$ (-0.28 eV), and $\text{Hf}_{\text{NbII}}\text{Si}_{\text{SiII}}$ (-0.48 eV), and $\text{Zr}_{\text{NbII}}\text{B}_{\text{SiII}}$



(-0.27 eV) at $X_{\text{NbII}}Y_{\text{SiII}}$ sites. Fig. 9 shows the E_{DS} of stable $X_{\text{Nb}}Y_{\text{Si}}@ \beta\text{-Nb}_5\text{Si}_3$ predicted by DFT and ML. The comparison shows that the trends predicted by the ML models were qualitatively consistent with those of DFT. The MAE and RMSE of E_{DS} of $\beta\text{-Nb}_5\text{Si}_3$ are 283.03 meV and 347.58 meV, respectively, comparable with those of $\alpha\text{-Nb}_5\text{Si}_3$. Notably, the prediction results for the $\text{Hf}_{\text{NbII}}\text{B}_{\text{SiII}}$, $\text{Ti}_{\text{NbII}}\text{B}_{\text{SiII}}$, $\text{Ti}_{\text{NbII}}\text{B}_{\text{SiII}}$, and $\text{Zr}_{\text{NbII}}\text{B}_{\text{SiII}}$ systems exhibit significant discrepancies. The larger atomic radii of Hf and Zr atoms tend to favor occupying the Nb_{II} sites, whereas the smaller atomic radius of Ti favors occupancy of the Nb_{I} sites. Additionally, the smaller B atoms tend to occupy the densely packed Si_{I} sites. These atomic site preferences in the Nb_5Si_3 phases are consistent with the reported first-principles calculations⁴¹. The reliability of prediction is acceptable given that the trained ML models were directly applied across the different crystal structures without any modification of parameters.

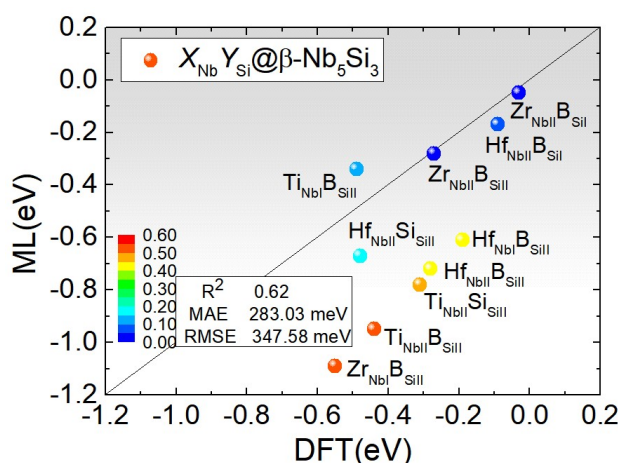


Fig. 9 Double-site substitution energies (E_{DS}) of the stable double-site substitution systems $X_{\text{Nb}}Y_{\text{Si}}@ \beta\text{-Nb}_5\text{Si}_3$ predicted by the ML models ($\text{CE}_{\text{AET}}\text{-SVR}$) and DFT. The colored scale bar indicates the absolute errors from low (in blue) to high (in red).

4 Conclusions

To develop a general feature model for complex crystal structures in machine learning studies, we introduced a Center-Environment feature model with Atomic Environment Type (CE_{AET}) to define the environment of atoms. The ML- CE_{AET} models proved to be effective, efficient, and transferable in predicting the alloying effects on the structural stability of $\alpha/\beta\text{-Nb}_5\text{Si}_3$ in NbSi-based superalloys. Comparisons between various CE construction methods revealed that: (1) The AET definition of environment atoms (CE_{AET}) outperforms the nearest neighbor-based approach (CE_{NN}). (2) The



reciprocal distance weighting function improved the performance of linear combinations of elementary features. (3) The SVR algorithm slightly outperformed RF in predicting substitution energies.

The optimized CE_{AET}-SVR models predicted the E_{DS} of α -Nb₅Si₃ with a MAE of 329 meV. Direct predictions on untrained β -Nb₅Si₃ indicated that Ti, Zr, and Hf prefer to occupy Nb sites, while B and Al tend to occupy Si sites. These machine learning predictions were further validated by first-principles calculations, demonstrating the reliable transferability of ML predictions using CE feature models.

This study demonstrated that non-deep machine learning models using CE feature representations, based on a small computational dataset, possess the predictive capability to study complex crystal structures with low symmetry and exhibit good transferability to new elements and structures. The achievement of CE feature models can be attributed to the pre-defined attention mechanism in feature engineering, leading to a better accuracy with less data requirement. Different from traditional feature engineering, the CE feature realizes a form of attention-driven information filtering through physical structure constraints, rather than simple empirical feature concatenation. Compared with deep learning attention, in scenarios with limited data, physical priors serve as substitutes for data-driven weight learning, enhancing model reliability and interpretability. This CE-based ML approach provides an efficient computational tool for the compositional design of multi-component engineering alloys.

Acknowledgments

This work was financially supported by the National Natural Science Foundation of China (Nos. 52373227, 52201016, and 91641128) and National Key R&D Program of China (Nos. 2017YFB0701502, 2017YFB0702901, and 2023YFB4606200). This work was also supported by the Shanghai Technical Service Center for Advanced Ceramics Structure Design and Precision Manufacturing (No. 20DZ2294000), Key Program of Science and Technology of Yunnan Province (No. 202302AB080020), and Shanghai Technical Service Center of Science and Engineering Computing, Shanghai University. The authors acknowledge the Beijing Super Cloud Computing Center, Hefei Advanced Computing Center, and Shanghai University for providing HPC resources.



1

2 Author contributions

3 Yuchao Tang: Methodology, Software, Investigation, Data curation, Visualization,
4 Writing - Original Draft; Bin Xiao: Methodology, Software; Shuizhou Chen: Software,
5 Validation; Quan Qian: Supervision, Validation; Yi Liu: Conceptualization,
6 Methodology, Funding, Resource, Supervision, Writing - Review & Editing.

7

8 Conflicts of interest

9 The authors declare no conflicts of interest.

10

11 Supplementary material

12 The supplementary materials in this paper can be found at: <http://xxx>



References

1. Perepezko JH. The hotter the engine, the better. *Science*. 2009;326(5956):1068-1069. doi:10.1126/science.1179327
2. Pollock TM. Alloy design for aircraft engines. *Nat Mater*. 2016;15(8):809-815. doi:10.1038/nmat4709
3. Liu W, Huang S, Ye C, et al. Progress in Nb-Si ultra-high temperature structural materials: A review. *J Mater Sci Technol*. 2023;149:127-153. doi:10.1016/j.jmst.2022.11.022
4. Sims CT. Niobium in superalloys: a perspective. *High Temp Technol*. 1984;2(4):185-201. doi:10.1080/02619180.1984.11753263
5. Bewlay BP, Jackson MR, Zhao JC, Subramanian PR, Mendiratta MG, Lewandowski JJ. Ultrahigh-temperature Nb-Silicide-based composites. *MRS Bull*. 2003;28(9):646-653. doi:10.1557/mrs2003.192
6. Vellios N, Tsakiroopoulos P. The role of Fe and Ti additions in the microstructure of Nb–18Si–5Sn silicide-based alloys. *Intermetallics*. 2007;15(12):1529-1537. doi:10.1016/j.intermet.2007.06.001
7. Zhang S, Shi X, Sha J. Microstructural evolution and mechanical properties of as-cast and directionally-solidified Nb-15Si-22Ti-2Al-2Hf-2V-(2, 14) Cr alloys at room and high temperatures. *Intermetallics*. 2015;56:15-23. doi:10.1016/j.intermet.2014.07.012
8. Qiao Y, Guo X, Zeng Y. Study of the effects of Zr addition on the microstructure and properties of Nb-Ti-Si based ultrahigh temperature alloys. *Intermetallics*. 2017;88:19-27. doi:10.1016/j.intermet.2017.04.008
9. Zhang S, Guo X. Alloying effects on the microstructure and properties of Nb–Si based ultrahigh temperature alloys. *Intermetallics*. 2016;70:33-44. doi:10.1016/j.intermet.2015.12.002
10. Shu J, Dong Z, Zheng C, et al. High-throughput experiment-assisted study of the alloying effects on oxidation of Nb-based alloys. *Corros Sci*. 2022;204:110383. doi:10.1016/j.corsci.2022.110383
11. Geng T, Li C, Bao J, Zhao X, Du Z, Guo C. Thermodynamic assessment of the Nb–Si–Ti system. *Intermetallics*. 2009;17(5):343-357. doi:10.1016/j.intermet.2008.11.011
12. Zhao JC, Jackson MR, Peluso LA. Determination of the Nb–Cr–Si phase diagram using diffusion multiples. *Acta Mater*. 2003;51(20):6395-6405. doi:10.1016/j.actamat.2003.08.007
13. Shao G. Thermodynamic assessment of the Nb–Si–Al system. *Intermetallics*. 2004;12(6):655-664. doi:10.1016/j.intermet.2004.03.011
14. Yang Y, Chang YA, Zhao JC, Bewlay BP. Thermodynamic modeling of the Nb–Hf–Si ternary system. *Intermetallics*. 2003;11(5):407-415. doi:10.1016/S0966-9795(03)00021-9
15. Li Y, Li C, Du Z, Guo C. Thermodynamic optimization of the Nb–Si–W ternary system. *Calphad*. 2013;43:112-123. doi:10.1016/j.calphad.2013.04.004
16. Wei W, Wang Q, Chen RR, Zheng CW, Su YQ. Enhancement of comprehensive properties of Nb–Si based in-situ composites by Ho rare earth doping. *Rare Met*. 2024;43(9):4508-4520. doi:https://doi.org/10.1007/s12598-024-02765-y
17. Huang YL, Jia LN, Kong B, Guo YL, Wang N. Microstructure and room temperature fracture toughness of Nb–Si-based alloys with Sr addition. *Rare Met*. 2024;43(8):3904-3912. doi:https://doi.org/10.1007/s12598-018-1141-8
18. Guo H, Guo X. Microstructure evolution and room temperature fracture toughness of an integrally directionally solidified Nb–Ti–Si based ultrahigh temperature alloy. *Scr Mater*.



- 2011;64(7):637-640. doi:10.1016/j.scriptamat.2010.12.008
19. Chen Y, Shang JX, Zhang Y. Bonding characteristics and site occupancies of alloying elements in different Nb₅Si₃ phases from first principles. *Phys Rev B*. 2007;76(18):184204. doi:10.1103/PhysRevB.76.184204
20. Xu X, Zeng W, Zhu SH, et al. Influences of vacancy concentration and Al substitution on structural, electronic, and elastic properties of Nb₅Si₃ from first-principles calculations. *Phys Status Solidi B*. 2021;258(5):2000591. doi:10.1002/pssb.202000591
21. Guo B, Xu J, Lu XL, Jiang S, Munroe P, Xie ZH. Electronic structure, mechanical and physical properties of Ag alloyed α -Nb₅Si₃: First-principles calculations. *Phys B Condens Matter*. 2019;564:80-90. doi:10.1016/j.physb.2019.04.013
22. Papadimitriou I, Utton C, Tsakiroopoulos P. The impact of Ti and temperature on the stability of Nb₅Si₃ phases: a first-principles study. *Sci Technol Adv Mater*. 2017;18(1):467-479. doi:10.1080/14686996.2017.1341802
23. Xu W, Han J, Wang C, et al. Temperature-dependent mechanical properties of alpha-/beta-Nb₅Si₃ phases from first-principles calculations. *Intermetallics*. 2014;46:72-79. doi:10.1016/j.intermet.2013.10.027
24. Shi S, Zhu L, Jia L, Zhang H, Sun Z. Ab-initio study of alloying effects on structure stability and mechanical properties of α -Nb₅Si₃. *Comput Mater Sci*. 2015;108:121-127. doi:10.1016/j.commatsci.2015.06.019
25. Kang Y, Han Y, Qu S, Song J. Effects of alloying elements Ti, Cr, Al, and Hf on β -Nb₅Si₃ from first-principles calculations. *Chin J Aeronaut*. 2009;22(2):206-210. doi:10.1016/S1000-9361(08)60088-6
26. Hart GLW, Mueller T, Toher C, Curtarolo S. Machine learning for alloys. *Nat Rev Mater*. 2021;6(8):730-755. doi:10.1038/s41578-021-00340-w
27. Liu Y, Wang J, Xiao B, Shu J tao. Accelerated development of hard high-entropy alloys with data-driven high-throughput experiments. *J Mater Inform*. 2022;2:3. doi:10.20517/jmi.2022.03
28. Liu G, Jia L, Kong B, Guan K, Zhang H. Artificial neural network application to study quantitative relationship between silicide and fracture toughness of Nb-Si alloys. *Mater Des*. 2017;129:210-218. doi:10.1016/j.matdes.2017.05.027
29. Xi S kun, Yu J xin, Bao L ke, et al. Machine learning-accelerated first-principles predictions of the stability and mechanical properties of L1₂-strengthened cobalt-based superalloys. *J Mater Inform*. 2022;2(3):15.
30. Witman MD, Schindler P. MatFold: systematic insights into materials discovery models' performance through standardized cross-validation protocols. *Digit Discov*. Published online 2025;10.1039/D4DD00250D. doi:10.1039/D4DD00250D
31. Li Y, Xiao B, Tang Y, et al. Center-environment feature model for machine learning study of spinel oxides based on first-principles computations. *J Phys Chem C*. 2020;124(52):28458-28468. doi:10.1021/acs.jpcc.0c06958
32. Wang X, Xiao B, Li Y, Tang Y, Liu Y. First-principles based machine learning study of oxygen evolution reactions of perovskite oxides using a surface center-environment feature model. *Appl Surf Sci*. 2020;531:147323. doi:10.1016/j.apsusc.2020.147323
33. Guo J, Xiao B, Li Y, et al. Machine learning aided first-principles studies of structure stability of Co₃(Al, X) doped with transition metal elements. *Comput Mater Sci*. 2021;200:110787. doi:10.1016/j.commatsci.2021.110787

View Article Online
DOI: 10.1039/D5DD00079C



34. Chen R, Liu F, Tang Y, et al. Combined first-principles and machine learning study of the initial growth of carbon nanomaterials on metal surfaces. *Appl Surf Sci.* 2022;586:152762. doi:10.1016/j.apsusc.2022.152762
35. Li Y, Zhu R, Wang Y, Feng L, Liu Y. Center-environment deep transfer machine learning across crystal structures: from spinel oxides to perovskite oxides. *Npj Comput Mater.* 2023;9(1):109. doi:10.1038/s41524-023-01068-7
36. Li Y, Zhang X, Li T, Chen Y, Liu Y, Feng L. Accelerating materials discovery for electrocatalytic water oxidation via center-environment deep learning in spinel oxides. *J Mater Chem A.* 2024;12(30):19362-19377. doi:10.1039/D4TA02771J
37. Louis SY, Zhao Y, Nasiri A, et al. Graph convolutional neural networks with global attention for improved materials property prediction. *Phys Chem Chem Phys.* 2020;22(32):18141-18148. doi:10.1039/D0CP01474E
38. Schmidt J, Pettersson L, Verdozzi C, Botti S, Marques MAL. Crystal graph attention networks for the prediction of stable materials. *Sci Adv.* 2021;7(49):7948. doi:10.1126/sciadv.abi7948
39. Choudhary K, DeCost B. Atomistic Line Graph Neural Network for improved materials property predictions. *Npj Comput Mater.* 2021;7(1):185. doi:10.1038/s41524-021-00650-1
40. Vasylenko A, Antypov D, Schewe S, et al. Digital features of chemical elements extracted from local geometries in crystal structures. *Digit Discov.* 2025;4(2):477-485. doi:10.1039/D4DD00346B
41. Tang Y, Xiao B, Chen J, et al. Multi-component alloying effects on the stability and mechanical properties of Nb and Nb–Si alloys: a first-principles study. *Metall Mater Trans A.* 2023;54(2):450-472. doi:10.1007/s11661-022-06868-y
42. Villars P, Cenzual K, Gladyshevskii R, Iwata S. *Pauling File: Toward a Holistic View*. Materials Informatics; 2019.
43. Schütt KT, Glawe H, Brockherde F, Sanna A, Müller KR, Gross EKV. How to represent crystal structures for machine learning: Towards fast prediction of electronic properties. *Phys Rev B.* 2014;89(20):205118. doi:10.1103/PhysRevB.89.205118
44. Ward L, Liu R, Krishna A, et al. Including crystal structure attributes in machine learning models of formation energies via Voronoi tessellations. *Phys Rev B.* 2017;96(2):024104. doi:10.1103/PhysRevB.96.024104
45. Ouyang R, Curtarolo S, Ahmetcik E, Scheffler M, Ghiringhelli LM. SISSO: A compressed-sensing method for identifying the best low-dimensional descriptor in an immensity of offered candidates. *Phys Rev Mater.* 2018;2(8):083802. doi:10.1103/PhysRevMaterials.2.083802
46. Shi B, Zhou Y, Fang D, et al. Estimating the performance of a material in its service space via Bayesian active learning: a case study of the damping capacity of Mg alloys. *J Mater Inform.* 2022;2(2):8. doi:10.20517/jmi.2022.06
47. Andrew S. Database on properties of chemical elements. Database on properties of chemical elements. 2021. <http://phases.imet-db.ru/elements/mendel.aspx?main=1>
48. Ducker H, Burges C, Kaufman L, Smola A, Vapnik V. Support vector regression machines. *Adv Neural Inf Process Syst.* 1997;28(7):779-784.
49. Leo B. Random forests. *Mach Learn.* 2001;45(1):5-32. doi:10.1023/A:1010933404324
50. Daams J, Vanvucht J, Villars P. Atomic-environment classification of the cubic “Intermetallic” structure types. *J Alloys Compd.* 1992;182(1):1-33. doi:10.1016/0925-8388(92)90570-Y
51. Villars P, Cenzual K, eds. β -Nb₅Si₃ Crystal Structure: Datasheet from “PAULING FILE



Multinaries Edition – 2012” in Springer Materials. Springer-Verlag Berlin Heidelberg & Material Phases Data System (MPDS), Switzerland & National Institute for Materials Science (NIMS), Japan https://materials.springer.com/isp/crystallographic/docs/sd_0533318

[View Article Online](#)
DOI: 10.1039/D5DD00079C



[View Article Online](#)

1661-022-
1661-022-9/D5DD00079C

